RSC Advances

PAPER

View Article Online
View Journal | View Issue

Cite this: *RSC Adv.*, 2023, **13**, 24385

Preparation of $Li_3V_2(PO_4)_3$ as cathode material for aqueous zinc ion batteries by a hydrothermal assisted sol–gel method and its properties

Shiyu Cao,[a] Yanhong Xiang,*[a] Qiuling Zou,[a] Youliang Jiang,*[b] Hanzhang Zeng,[a] Jian Li,[a] Jianhua Wu,[a] Xiangsi Wu,[c] Xianwen Wu[c] and Lizhi Xiong*[d]

To alleviate the depletion of lithium resources and improve battery capacity and rate capacity, the development of aqueous zinc-ion batteries (AZIBs) is crucial. The open channels monoclinic structure $Li_3V_2(PO_4)_3$ is conducive to the transfer and diffusion of guest ions, making it a promising cathode material for AZIBs. Therefore, in this study, nanoneedles and particles $Li_3V_2(PO_4)_3$ cathode materials for AZIBs were prepared by a hydrothermal assisted sol–gel method, and the effect of synthesized pH values was studied. XRD results show that all samples had the monoclinic structure, and the $Li_3V_2(PO_4)_3$ sample prepared at pH = 7 exhibits (LVP-pH7) the highest peak tips and narrowest peak widths. SEM images demonstrate that all samples have the morphology character of randomly oriented needles and irregular particles, with the LVP-pH7 sample having more needle-like particles that contribute to ion diffusion. EDS results show uniform distribution of P, V, and O elements in the LVP-pH7 sample, and no obvious aggregation phenomenon is observed. Electrochemical tests have shown that the LVP-pH7 sample exhibits excellent cycling performance (97.37% after 50 cycles at 200 mA g^{-1}) and rate ability compared to other samples. The CV test results showed that compared with other samples, the LVP-pH7 sample had the most excellent ionic diffusion coefficient (2.44×10^{-12} cm^2 s^{-1}). Additionally, the R_{ct} of LVP-pH7 is the lowest (319.83 Ω) according to the findings of EIS and Nyquist plot fitting, showing a decreased charge transfer resistance and raising the kinetics of the reaction.

Received 20th March 2023
Accepted 7th August 2023

DOI: 10.1039/d3ra01816d

rsc.li/rsc-advances

1. Introduction

With the continued use of fossil fuels and the slow intensification of the greenhouse effect, energy scarcity and environmental pollution have become two major challenges for the survival and development of human society, and people are increasingly interested in novel energy sources.[1,2] Currently, lithium-ion batteries (LIBs) occupy the commercial market of rechargeable batteries and have become the main mobile energy source.[3,4] However, in recent years, with the rise in the price of lithium metal sheets and the frequent occurrence of safety problems in LIBs, the future market of LIBs is worrying.[5] At the same time, AZIBs are considered as the ideal green energy system for the next generation due to their advantages such as safe water-based systems, low price of zinc sheets (negative electrodes), abundant resources, low redox potential (−0.76 V *vs.* standard hydrogen electrode, SHE), and high energy density.[5–7] Therefore, the development of alternative water energy storage systems is crucial.[3] The cathode material is a key factor in determining the final performance of AZIBs.[8] The de-insertion process of zinc ions in AZIBs will interact with the cathode materials, so suitable embedding materials are rare. Since its conception, finding the cathode materials that can match the zinc anode is the key and difficult point of research.[9] So far, manganese-based oxides,[9] vanadium-based materials,[10] Prussian blue analogs,[11] polyanion compound,[12,13] chevrel phase compound,[14] and organic compound[15] have been reported as cathode materials for AZIBs. The vanadium-based materials are not limited by low specific capacity and deliver excellent electrochemical performance.[9] Among them, phosphate (such as polyanionic type and NASICON type phosphate) has the advantages of high structural strength and interconnected three-dimensional channels, which can form flexible active sites conducive to the internal transport of Zn^{2+}.[1] More importantly, there is enough space in the structure of the monoclinic $Li_3V_2(PO_4)_3$ compound to conduct Zn^{2+}.[16,17] Therefore, $Li_3V_2(PO_4)_3$ can be used to prepare AZIBs.

Currently, in order to solve the problems of poor electronic conductivity, low cycling stability, and structural degradation in aqueous electrolytes of $Li_3V_2(PO_4)_3$.[18,19] A large number of researchers employed a lot of synthetic methods to promote the

[a]*School of Physics and Electrical Engineering, Jishou University, Jishou 416000, P. R. China. E-mail: yhx@jsu.edu.cn*

[b]*Loudi Technician Institute, Loudi 417100, P. R. China*

[c]*School of Chemistry and Chemical Engineering, Jishou University, Jishou 416000, P. R. China*

[d]*School of Pharmacy, Jishou University, Jishou 416000, P. R. China*

morphology of materials.[18] Among them, although high temperature solid phase technology has the benefits of ease of use and cheap expense,[20] it is more likely to generate pollutants. Although the coprecipitation technique has the benefits of a quick reaction time, customizable morphology, and low reaction temperature,[21] it is challenging to prepare. The materials prepared by the sol–gel method have uniform particle size distribution, high purity, and can achieve molecular level mixing, and are widely used to prepare metal oxide materials. The hydrothermal technique is a way of producing materials in an enclosed pressure tank by dissolving and recrystallizing water as a solvent and powder.[22] When compared to other powder preparation techniques, the hydrothermal method has the following advantages: full grain growth, small particle size, homogeneous distribution, light particle aggregation, inexpensive raw materials, and ease of obtaining suitable stoichiometry and crystal shape.[23] Therefore, if the hydrothermal method is used to dissolve and recrystallize the aqueous materials first, and then combined with the sol–gel method to prepare the micro nano $Li_3V_2(PO_4)_3$ precursor materials. It makes the grain of $Li_3V_2(PO_4)_3$ develop completely and the structure is relatively stable, which can improve the cyclic stability of the material. Meanwhile, because $Li_3V_2(PO_4)_3$ materials may behave differently under varying pH conditions,[24] so it is important to understand the effect of pH parameters in detail on the structure and performance of $Li_3V_2(PO_4)_3$. There has been no comprehensive investigation of the impact of pH on $Li_3V_2(PO_4)_3$.

As a result, the $Li_3V_2(PO_4)_3$ sample was generated using a hydrothermal aided sol–gel process in this research, and the effect of synthesized pH settings on the structural morphology and electrochemical performance of $Li_3V_2(PO_4)_3$ cathode materials was systematically studied during the synthesis process. This auxiliary method is expected to regulate the size and shape of $Li_3V_2(PO_4)_3$ powder, endowing the $Li_3V_2(PO_4)_3$ with a consistent nano size and a continuous electrons channel, so significantly improving the rate capability and cycle stability of $Li_3V_2(PO_4)_3$. This work has the potential to make $Li_3V_2(PO_4)_3$ a strong candidate for the positive electrode material of aqueous zinc ion batteries.

2. Materials and methods

As shown in Fig. 1, a new hydrothermal assisted sol–gel method was used to prepare monoclinic $Li_3V_2(PO_4)_3$ positive electrode materials. Lithium acetate dihydrate ($CH_3COOLi\cdot 2H_2O$), ammonium metavanadate (NH_4VO_3), ammonium dihydrogen phosphate ($NH_4H_2PO_4$) were completely dissolved in deionized water according to the stoichiometric ratio to obtain 0.5 M metal ion mixed solution. Citric acid ($C_6H_8O_7$) was used as binder to prepare 0.5 M solution. Secondly, add $C_6H_8O_7$ solution slowly to the above mixed solution, and stirred at a constant temperature of 60 °C for 4 h. During this period, ammonia ($NH_3\cdot H_2O$) was used to adjust the pH value of the solution. After stir, the solution is transferred to a 100 ml reactor and reacted at 180 °C for 12 h. The solution was removed and cooled naturally, and finally the cooled solution was stirred into a gel at 80 °C to obtain the precursor. All the chemicals used above are from Aladdin chemical reagents.

Fig. 1 The illustration of synthesis processes for $Li_3V_2(PO_4)_3$ cathode materials.

To analyze the effect of pH (5, 6, 7, 8) on the material, the pH of the precursor was adjusted to pH 5, pH 6, pH 7, and pH 8 by $NH_3\cdot H_2O$. The prepared gel precursor was then heated in a tubular furnace to 350 °C using a flowing N_2 atmosphere and held for 5 h to remove H_2O, NH_3 and CO_2 from the decomposition of the organic components, and then heated at 800 °C for 10 h. The $Li_3V_2(PO_4)_3$ cathode materials were obtained. We labeled the $Li_3V_2(PO_4)_3$ cathode materials obtained by calcination of different pH precursors as LVP-pH5, LVP-pH6, LVP-pH7 and LVP-pH8, respectively.

2.1 Characterization

X-ray diffraction (XRD, Rigaku 2500, Japan) with Cu-Kα (λ = 0.15406 nm) radiation from 10° to 70° was used to examine the crystal structure of materials. Scanning electron microscopy was used to analyze the morphology and particle (SEM, Zeiss Sigma 300). An EDS (SEM-EDS, Oxford Xplore 30) was used to determine the element distribution of the prepared materials. The surface chemical composition and valence state of samples were investigated by X-ray photoelectron spectroscopy (XPS, Thermofisher Escalab 250Xi, USA).

2.2 Electrochemical test

The preparation process of $Li_3V_2(PO_4)_3$ positive plate mainly includes the following steps: first, $Li_3V_2(PO_4)_3$ powder, acetylene black and polyvinylidene fluoride (PVDF) were mix and grind according to the mass ratio of 7 : 2 : 1 to obtain the mixed slurry. Then the slurry is applied to a 14 mm stainless steel wire disc. Finally, the discs are dried at 80 °C for 12 h to obtain 14 mm $Li_3V_2(PO_4)_3$ cathode sheets. Zn foil was used as the anode and $Li_3V_2(PO_4)_3$ as the cathode for the CR-2016 coin-type cells, which were then separated by a glass fiber separator with an aqueous electrolyte (2 M $ZnSO_4$ + 1 M Li_2SO_4). At room temperature, the CT2001A LAND (Wuhan, China) battery test system was used to test the rate performance, cycle performance and charge–discharge performance of the material. The voltage range of the test is 0.7–1.7 V, and the method of discharging before charging is adopted. Cyclic voltammetry (CV) and electrochemical impedance spectroscopy (EIS) were tested using an

electrochemical workstation (CH1660E, Shanghai). The scan rate of CV was 0.5, 0.3, 0.2, 0.1 mV s^{-1}, and the voltage window range was 0.7–1.7 V. The frequency range of EIS was 0.01 Hz–100 kHz.

3. Results and discussion

The crystal structures of $Li_3V_2(PO_4)_3$ are monoclinic and rhombic, but the thermodynamic instability of the rhombic crystal structure makes it difficult to create. The monoclinic $Li_3V_2(PO_4)_3$ is thermodynamically stable, its synthesis is relatively simple, and it also has a large capacity.[25] At present, monoclinic $Li_3V_2(PO_4)_3$ cathode materials have emerged as a research focus. Fig. 2a displays the X-ray diffraction (XRD) patterns of the acquired $Li_3V_2(PO_4)_3$ samples at various pH levels. The NASICON $Li_3V_2(PO_4)_3$ structure is an open framework made up of VO_6 octahedral and PO_4 tetrahedral sharing oxygen vertex, as shown in Fig. 2b. XRD results demonstrated that the main characteristic peaks of the all samples at around 20.9°, 24.5° and 29.5° are indexed to (020), (121), (220) facets of $Li_3V_2(PO_4)_3$ (JCPDS no. 72-7074), which reflects a high degree of preferred orientation along *c* axis.[26] All of the diffraction peaks belong to the $P2_{1/n}$ space group of monoclinic $Li_3V_2(PO_4)_3$.[27] The peak shape of the materials is sharp, and there is no obvious secondary phase or impurity phase in the XRD spectrum, thus indicating that all the samples synthesized are of high purity. It shows that we have successfully prepared $Li_3V_2(PO_4)_3$ materials. In addition, it was found that the crystallinity of $Li_3V_2(PO_4)_3$ gradually increases with the increase of pH value. Among them, the LVP-pH7 sample is demonstrated by the narrowed full width half maximum of peaks and by the increased peak intensity. The $Li_3V_2(PO_4)_3$ samples showed higher peak tips and narrower peak widths at pH = 7. This shows that the $Li_3V_2(PO_4)_3$ material synthesized under neutral conditions has higher purity and better crystal structure. When the pH value reaches up to 8, thanks to the increase in NH_4^+ ion in mixed solution, the reaction rate of citric acid complexing with metal ions decrease, so it may lead to poor crystallinity. In addition, based on the XRD data of the samples, the average crystallite sizes of all samples were calculated using the Debye Scherrer formula (as shown in eqn (1)).[28] The average crystallite sizes of all samples were $D_{LVP\text{-}pH5}$ = 99.48 nm, $D_{LVP\text{-}pH6}$ = 14.75 nm, $D_{LVP\text{-}pH7}$ = 24.43 nm, and $D_{LVP\text{-}pH8}$ = 26.37 nm, respectively. It can be seen that materials prepared under nearly neutral conditions have smaller grain sizes.

$$D = \frac{K\lambda}{\beta \cos \theta} \quad (1)$$

Parameter meaning: *D*: crystallite sizes, nm; *K*: Scherrer constant, $K = 0.89$; λ: the X-ray wavelength, for Cu·Kα, λ = 0.15406; β: half peak width of diffraction angle; θ: diffraction angle.

To further study the elemental compositions of LVP-pH7 sample, XPS test was adopted. Fig. 3 shows the XPS image of the LVP-pH7 sample. The signals of carbon, vanadium, phosphorus, lithium and oxygen elements can be clearly detected in the XPS curve (Fig. 3a). The C-spectrum of LVP-pH7 material is shown in Fig. 3b. The C1s spectrum at binding energy value of 284.8 eV is corresponded to sp2 C–C bonds, This indicates that citrate decomposes into carbon during the calcination process, and there is residual carbon present in $Li_3V_2(PO_4)_3$.[29] The V2p spectrum presented in Fig. 3c possesses two obvious peaks located at around 517.5 and 524.7 eV, representing the $V2p_{3/2}$ and $V2p_{1/2}$ respectively,[16] The observed binding energy values correspond to V^{3+} in LVP-pH7 sample, suggesting the successful reduction of V^{5+} to V^{3+}.[25]

To study the morphology of all samples, the morphology of the $Li_3V_2(PO_4)_3$ materials are investigated by using a scanning electron microscope (SEM). Fig. 4 (a–d) shows the SEM images of LVP-pH5, LVP-pH6, LVP-pH7 and LVP-pH8 samples, respectively. All samples displayed randomly oriented needles and irregular particles. The morphology of this composite is not only conducive to the contact between electrolyte and particles, but also accelerate electron transport through randomly oriented needles along nanorods simultaneously.[30] Further observations revealed, with the increase of pH value, the material particles gradually become smaller, and the number of needles changed obviously as the pH value increased. Especially, there are quite a multiple randomly oriented needles with a diameter of 50 to 100 nm in the LVP-pH7 sample Fig. 4c, but when the pH increased to 8, the number of such needles decreased instead. These special needles are conducive to electrolyte penetration and rapid ion diffusion, which can overcome the problem of poor ion diffusion of phosphate compounds, reduce charge transfer resistance, reduce the transmission distance of lithium ions, and increase the diffusion rate of lithium ions, which is conducive to improving electrochemical performance. Fig. 4e and f shows the EDS element mapping of the LVP-pH7 sample. O, P, and V elements were uniformly distributed in the cathode material.

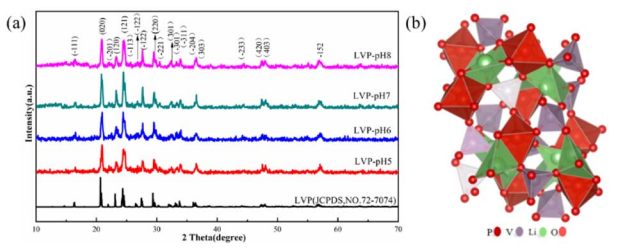

Fig. 2 (a) The X-ray diffraction (XRD) pattern of LVP-pH5, LVP-pH6, LVP-pH7, and LVP-pH8. (b) Schematic illustration of $Li_3V_2(PO_4)_3$ crystal structure.

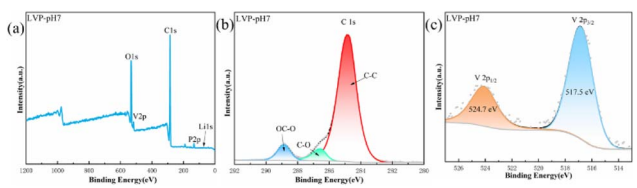

Fig. 3 (a) XPS survey curves of the fabricated LVP-pH7 sample; XPS spectra of LVP-pH7 samples: (b) C1s, and (c) V2p.

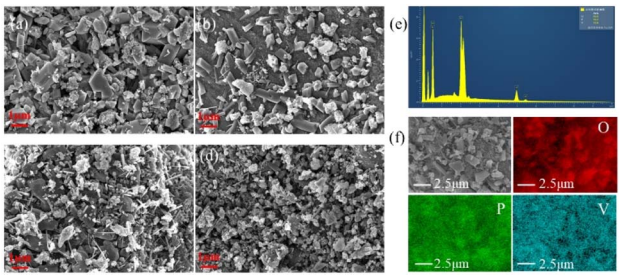

Fig. 4 The scanning electron microscopy (SEM) images of (a) LVP-pH5, (b) LVP-pH6, (c) LVP-pH7, and (d) LVP-pH8. (e and f) EDS element mapping of LVP-pH7.

In order to further explore the influence of pH value of synthesis conditions on the electrochemical properties of $Li_3V_2(PO_4)_3$ in AZIBs, the constant current charging–discharge test is carried out under a current density of 2C (200 mA g^{-1}) in a potential voltage range of 0.7–1.7 V (*vs.* Zn^{2+}/Zn). As shown in Fig. 5a–d, the charge and discharge plateaus of sample occur at 1.38 V, 1.33 V and 1.47 V, 1.41 V correspond to a series of phase transitions of $Li_3V_2(PO_4)_3 \leftrightarrow Li_2V_2(PO_4)_3 \leftrightarrow LiV_2(PO_4)_3$, resulting in a $V^{3+}/V^{4+}/V^{5+}$ ordering state.[31] The initial discharge capacities of the LVP-pH5, LVP-pH6, LVP-pH7 and LVP-pH8 samples are 52.81 mA h g^{-1}, 53.43 mA h g^{-1}, 68.35 mA h g^{-1} and 45.42 mA h g^{-1}, respectively. Different from LIBs, during the initial charge, few Li^+ are de-intercalated into the electrolytes, while Zn^{2+} are plated in the anode. During the discharge, Li^+ in electrolytes can provide an additional part of capacity. Due to the use of 2 M $ZnSO_4$ + 1 M Li_2SO_4 as the electrolyte, the Li^+ of electrolyte can provide additional partial capacity during the discharge process. The results of the second charge–discharge also verify this viewpoint. In Fig. 5a and b, the discharge specific capacity of the LVP-pH7 sample was significantly improved compared with the other samples. Which may be due to the presence of more randomly oriented needles in the LVP-pH7 sample, thereby increasing the contact area between the positive electrode material and the electrolyte. This can accelerate the ion removal/insertion, increase the active reaction sites, and thus increase the discharge specific capacity.

Fig. 6 shows the cycling performance and rate characteristics of LVP-pH5, LVP-pH6, LVP-pH7 and LVP-pH8 samples in AZIBs. The rate capacity test was increased by varying from 2C to 20C, and then returned to 2C. All samples showed good capacity retention and good stability. This could be due to the use of a hydrothermal aided sol–gel preparation technique, which results in a material with improved electrochemical performance. The discharge specific capacities of LVP-pH7 sample at different rates of 2C–20C are 65.91, 56.35, 50.57, 46.64, and 40.77 mA h g^{-1}, respectively. It is obvious that the LVP-pH7 sample shows the highest discharge specific capacity at all rates. Meanwhile, the samples capacity gradually increases when the pH increases from 5 to 7, but when the pH increased to 8, the capacity decreased instead, even lower than the LVP-pH5 sample. This may be due to the fact that neutral conditions are more conducive to the complexation reaction between citric acid and metal ions, thereby improving the crystallinity of the material, as well as produces more needles that contribute to ion transport. On the other hand, when the pH increases to 8, excessive NH^{4+} can lead to a decrease in the reaction rate of citric acid complexing with metal ions, leading to a decrease in crystallinity. Moreover, when the rate returned to 2C, the specific capacity of LVP-pH7 could still recover to 52.39 mA h g^{-1}, which was 80.77% of the initial capacity, much higher than the 42.61 mA h g^{-1} of LVP-pH5, the 41.87 mA h g^{-1} of LVP-pH6 and the 33.65 mA h g^{-1} of LVP-pH8. It can be seen from the figure that under the high current density of 2C, after 50 cycles, the specific capacity attenuation of LVP-pH7 is very small, and the capacity retention rate is high (remains at 97.37%). A large number of randomly oriented acicular and irregular particles in LVP-pH7 sample, which can improve the diffusion coefficient of guest ions in the material, and the unique structure can effectively alleviate the volume expansion of the material in the process of charging and discharging. And

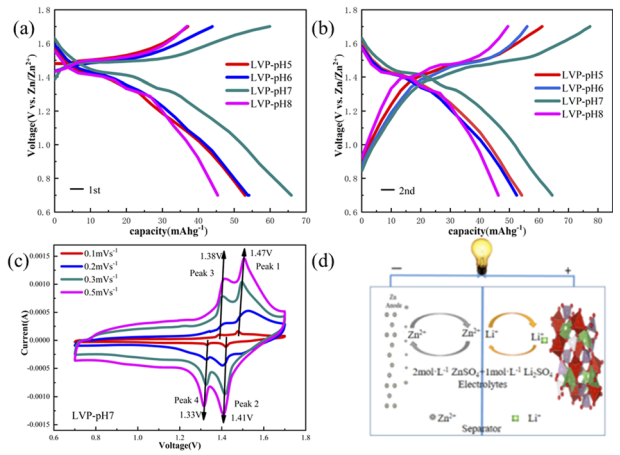

Fig. 5 (a) The initial charge/discharge curves of LVP-pH5, LVP-pH6, LVP-pH7 and LVP-pH8. (b) The second charge/discharge curves. (c) The CV curves of LVP-pH7 at different scan rates of 0.1–0.5 mV s^{-1}. (d) The operating principle of aqueous zinc ion battery.

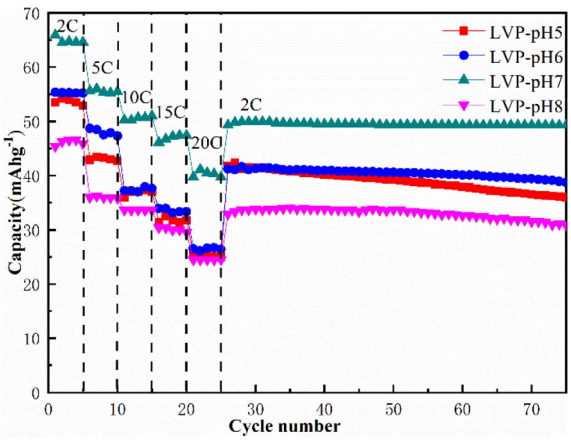

Fig. 6 The rate capabilities and cycle performances of LVP-pH5, LVP-pH6, LVP-pH7 and LVP-pH8.

quickly provide a certain amount of space for the guest (ion/electron), thus enhancing the rate characteristics and cycle performance of the material. In addition, compared with other AZIBs $Li_3V_2(PO_4)_3$ cathode materials, the discharge performance of $Li_3V_2(PO_4)_3$ materials prepared by hydrothermal assisted sol–gel method has been improved.[32–35]

Electrochemical impedance spectroscopy (EIS) was used to assess the kinetic characteristics of all $Li_3V_2(PO_4)_3$ samples. Fig. 7 shows the EIS plots for all samples. Use Zview fitting software to establish equivalent circuit. The Nyquist diagram of the electrode material consists of a semicircle in the high-frequency region and a slash line in the low-frequency region. The semi-circle in the high frequency region corresponds to the electrochemical reaction resistance and the double-layer capacitance of the electrode material, while the slash line in the low frequency region corresponds to the diffusion of ions, namely, Warburg diffusion. Charge-transfer resistance (R_{ct}) may be calculated from the semicircle in the high-frequency region, which corresponds to the resistance between the electrolyte and the $Li_3V_2(PO_4)_3$ electrode.[35,36] According to the fitting findings, the R_{ct} value of the LVP-pH7 sample (319.83 Ω) was substantially lower than that of the LVP-pH5 sample (515.95 Ω), the LVP-pH6 sample (413.96 Ω), and the LVP-pH8 sample (598.37 Ω). This result demonstrates that guest ion transfer is much easier inside the LVP-pH7 sample between the electrode and electrolyte, which may profit from the special morphology and structure of $Li_3V_2(PO_4)_3$ sample, which is beneficial to enhance the electrical conductivity and zinc ion diffusion coefficient of the material. This is consistent with the results of rate and cycle properties.

To analyze the redox process and ion diffusion rate in electrode reactions, the cyclic voltammetric tests were carried out on all samples between 0.7 V and 1.7 V (the scanning rates were 0.1, 0.2, 0.3 and 0.5 $mV \cdot s^{-1}$, scanning direction is positive scanning). The CV curves of LVP-pH5, LVP-pH6, and LVP-pH8 at different scanning rates are shown in Fig. 8, while the CV curves of LVP-pH7 are shown in Fig. 5c. We can clearly see that the CV curves of all samples show similar profiles with two reduction peaks and two oxidation peaks. The first oxidation peak of

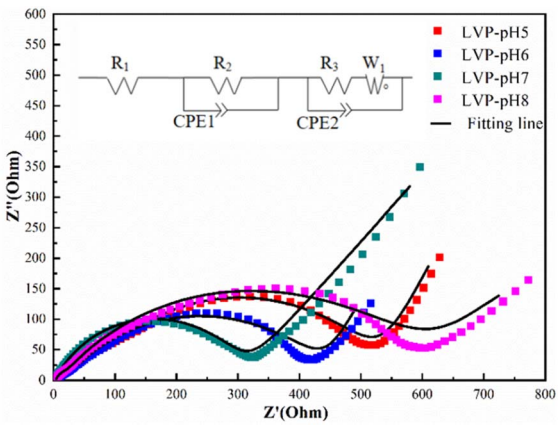

Fig. 7 The Nyquist plots of LVP-pH5, LVP-pH6, LVP-pH7 and LVP-pH8.

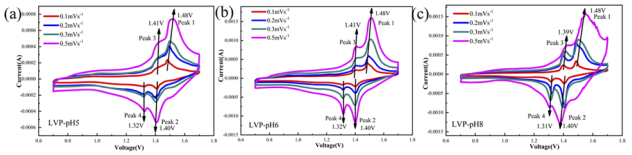

Fig. 8 The CV curves of (a) LVP-pH5, (b) LVP-pH6, (c) LVP-pH8 at different scan rates of 0.1–0.5 mV s^{-1}.

around 1.39 V during charge can be assigned to the extraction of first lithium ion with the oxidation of vanadium from V^{3+} to V^{3+}/V^{4+}. The second oxidation peak of around 1.48 V derived from the extraction of second lithium ion with the entire vanadium oxidation from V^{3+}/V^{4+} to V^{4+} in reaction.[37] In the subsequent discharge process, the first reduction peak of around 1.40 V can be detected, which is due to the initial re-insertion of lithium ion into $LiV_2(PO_4)_3$, but the re-insertion of zinc ion into the surface of the cathode electrode.[38] The second reduction peak near 1.33 V is attributed to the second lithium ion insertion.[39] This corresponds to the first charge/discharge curve in Fig. 5a. The CV curves of all samples show that as the scanning speed increases, the voltage difference between redox peaks gradually increases,[40] the height and size of redox peaks also increase, and the peak current also increases.[40] This means that irreversible behavior becomes more and more apparent at larger scanning rates. This is because lithium ions cannot be fully extracted/inserted/entered from the electrode during the time interval of high rate scanning, resulting in irreversible behavior.[37] In addition, the redox peaks of LVP-pH5, LVP-pH6, and LVP-pH8 samples had similar variation characteristics. Compared with LVP-pH7, the oxidation peaks of the other three samples significantly shifted towards higher potentials, while the corresponding reduction peaks shifted towards lower potentials. This would result in the LVP-pH7 sample having the smallest potential difference between oxidation peak and reduction peaks, which is related to the polarization and electrochemical reversibility of cathode materials.[41] This suggests that the LVP-pH7 sample have lower polarization and better electrochemical reversibility.[42,43] This result is consistent with the previous electrochemical performance analysis. The results indicate that $Li_3V_2(PO_4)_3$ has an interactive transformation mechanism, and lithium ions migrate reversibly into the cathode along with zinc ions platting/stripping at the anode during charge and discharge, to realize the reversible de-insertion/insertion of zinc ions. Zinc diffusion in the electrode is the rate-limiting step if the charge transfer at the interface is quick enough, and Randle–Sevcik[36] (2) may be used to compute the ion diffusion coefficient:

$$i_p = 2.69 \times 10^5 \times n^{3/2} A \times D^{1/2} C_0 \times V_{1/2} \quad (2)$$

where i_p is the peak current, n is the number of electrons per reactive species, A is the surface area of the electrode (here the geometric area of electrode 1.5385 cm^2), $D^{1/2}$ is the diffusion coefficient ($cm^2\ s^{-1}$) of Zn^{2+}, C_0 is the concentration of zinc ions (2 M) and $V^{1/2}$ is the scanning rate. According to the linear

fitting results of cyclic voltammetry in Fig. 9, the corresponding slope was calculated, and then the zinc ion diffusion coefficients are 1.92×10^{-13}, 1.37×10^{-12}, 2.44×10^{-12} and 1.17×10^{-12} ($cm^2\ s^{-1}$) for the LVP-pH5, LVP-pH6, LVP-pH7 and LVP-pH8 samples respectively. By comparing the CV results of all samples, it is found that LVP-pH7 sample have a good ion diffusion rate, which is consistent with the morphological characteristics and EIS results.

To get insight into the structural evolution process, in order to further discussed the effect of pH value on the crystal structure, morphology and electrochemical performance of the material. The cycling electrode were evaluated by *ex situ* XRD measurements. Fig. 10 shows the *ex situ* XRD patterns of LVP-pH7 sample under different charge states. Under different charge states, the characteristic peak strength of the LVP-pH7 sample after charging and discharging is slightly lower than that of the original LVP-pH7 material. However, the original monoclinic structure of the LVP-pH7 material basically maintains remains. Compared with the standard card, the peak values detected at 43° and 51° belong to the iron mesh current collector.[40] Throughout the charging and discharging process, Li^+ is embedded and detached from $Li_3V_2(PO_4)_3$, which leads to subtle structural changes of the material. As shown in Fig. 10b. For *ex situ* X-ray diffraction, no obvious Zn inserted diffraction peak can be detected in the charge or discharged electrodes. This *ex situ* XRD signal evolution of $Li_3V_2(PO_4)_3$ is similar to the observation in the LIBs.[37] As shown in Fig. 10a. By comparing the XRD with the standard card, it was found that point a at 1.7 V in Fig. 10a coincides with $LiV_2(PO_4)_3$, point b and c correspond to $Li_2V_2(PO_4)_3$ material, and point d corresponds to $Li_3V_2(PO_4)_3$ material. Point a–d corresponds to the discharge process of the battery, and is accompanied by the insertion of Li^+. Similarly, point e and f correspond to $Li_2V_2(PO_4)_3$ material, and point g has the same structure as point a, which is $LiV_2(PO_4)_3$. However, starting from d–g corresponds to the

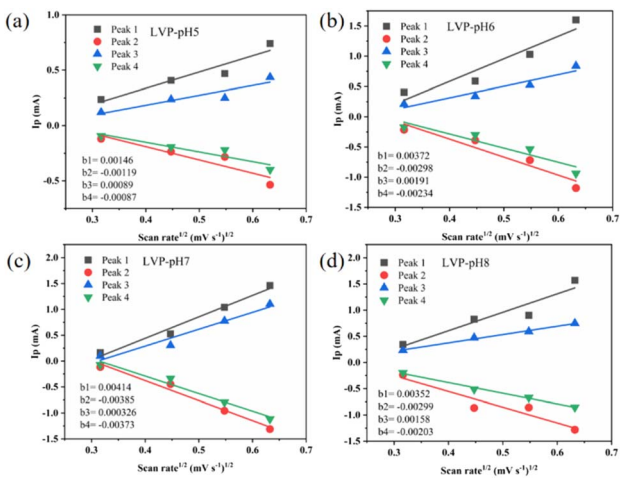

Fig. 9 The relationship between the current peaks and scan rate is based on the CV curves. (a) LVP-pH5, (b) LVP-pH6, (c) LVP-pH7 and (d) LVP-pH8.

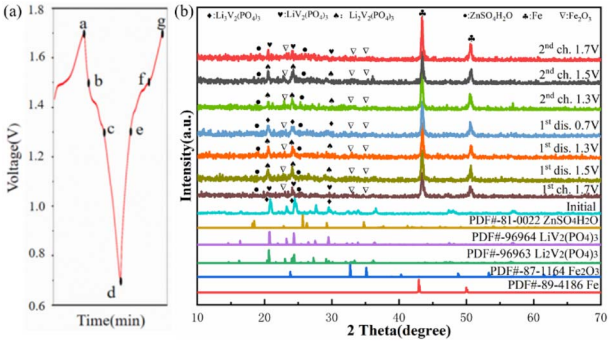

Fig. 10 The *ex situ* XRD patterns of LVP-pH7 at different charge state.

battery charging process, accompanied by the release of Li^+. As expected, from a–g after the charging and discharging process, the diffraction peaks are able to fully recover in the initial (point a) state. This indicates that the migration process of Li^+ is reversible. Furthermore, $Li_3V_2(PO_4)_3$ cathode material prepared by hydrothermal assisted sol–gel has good reversibility and structural stability.

4. Conclusions

In conclusion, we effectively developed and manufactured $Li_3V_2(PO_4)_3$ materials using an unique hydrothermal aided sol–gel process to enhance both electronic conductivity and zinc ion diffusivity. In addition, the effect of pH value on the morphology and electrochemical properties of $Li_3V_2(PO_4)_3$ materials was systematically studied. The XRD and SEM results show that all the samples we prepared have high crystallinity and show randomly oriented needle and irregular particles. The morphology of this composite is not only conducive to the contact between electrolyte and particles, but also accelerate electron transport through randomly oriented needles along nanorods simultaneously. Electrochemical test results indicated that adjusting pH value during the synthesis has an important effect on rate capability and cyclability. The LVP-pH7 sample with the increasing number of needle-like has importantly enhanced electrochemical performance, compared to the LVP-pH5, LVP-pH6 and LVP-pH8 samples. The capacity retention of the LVP-pH7 remains at 97.37% after the 50th cycle at 2C. Besides, the EIS data show the LVP-pH7 sample had a relatively smaller charge transfer resistance value and thus alleviates the diffusion pathways of ions and electrons. The CV fitting result indicated that the LVP-pH7 had a relatively greater ions diffusion rate, which is will correspond with the rate capability and EIS test results. The improved performance can be mainly attributed to these needles and particles in the LVP-pH7 sample because the existence of needles may reduce aggregation between aside structures, increase the special surface area for holding electrolyte. In general, when the pH value increases from 5 to 7, the various properties of $Li_3V_2(PO_4)_3$ materials also become better, but when the pH value increases to 8, the various properties decrease rapidly. This study provides a method and idea for preparing new AZIBs cathode materials.

Author contributions

Shiyu Cao: methodology, investigation, writing – original draft; Yanhong Xiang: conceptualization, investigation, writing – review & editing; Qiuling Zou: investigation, writing – original draft; Youliang Jiang: resources, investigation; Hanzhang Zeng: data curation; Jian Li: visualization, writing – review & editing; Jianhua Wu: data curation; Xianwen Wu: resources, visualization; Lizhi Xiong: validation.

Conflicts of interest

The authors declare that they have no known competing financial interests or personal relationships that could have appeared to influence the work reported in this paper.

Acknowledgements

This research was financially supported by the National Natural Science Foundation of China (No. 52264037, No. 52064014, No. 52265019 and No. 52064013), the Young Scientific and Technological Talents (Hejian) Project of Hunan Province (No. 2022RC1087), and the Outstanding Youth Funding program of Hunan Province (No. 2023JJ10033, 2022JJ40341), the National innovation training program for undergraduate (No. 202110531002), which were greatly appreciated.

Notes and references

1 T. Lv, Y. Peng, G. Zhang, S. Jiang, Z. Yang, S. Yang and H. Pang, How About Vanadium-Based Compounds as Cathode Materials for Aqueous Zinc Ion Batteries, *Adv. Sci.*, 2023, e2206907.

2 J. Yang, B. Yin, Y. Sun, H. Pan, W. Sun, B. Jia, S. Zhang and T. Ma, Zinc Anode for Mild Aqueous Zinc-Ion Batteries: Challenges, Strategies, and Perspectives, *Nanomicro Lett.*, 2022, **14**(1), 42.

3 Y. Cai, R. Chua, S. Huang, H. Ren and M. Srinivasan, Amorphous manganese dioxide with the enhanced pseudocapacitive performance for aqueous rechargeable zinc-ion battery, *Chem. Eng. J.*, 2020, **396**, 125221.

4 M. H. Alfaruqi, S. Islam, J. Gim, J. Song, S. Kim, D. T. Pham, J. Jo, Z. Xiu, V. Mathew and J. Kim, A high surface area tunnel-type α-MnO_2 nanorod cathode by a simple solvent-free synthesis for rechargeable aqueous zinc-ion batteries, *Chem. Phys. Lett.*, 2016, **650**, 64–68.

5 S. Chen, R. Lan, J. Humphreys and S. Tao, Salt-concentrated acetate electrolytes for a high voltage aqueous Zn/MnO_2 battery, *Energy Stor. Mater.*, 2020, **28**, 205–215.

6 M. Shi, P. Xiao, C. Yang, Y. Sheng, B. Wang, J. Jiang, L. Zhao and C. Yan, Scalable gas-phase synthesis of 3D microflowers confining MnO_2 nanowires for highly-durable aqueous zinc-ion batteries, *J. Power Sources*, 2020, **463**, 228209.

7 C. Wang, Y. Zeng, X. Xiao, S. Wu, G. Zhong, K. Xu, Z. Wei, W. Su and X. Lu, γ-MnO_2 nanorods/graphene composite as efficient cathode for advanced rechargeable aqueous zinc-ion battery, *J. Energy Chem.*, 2020, **43**, 182–187.

8 H. Tan, L. Xu, H. Geng, X. Rui, C. Li and S. Huang, Nanostructured $Li_3V_2(PO_4)_3$ Cathodes, *Small*, 2018, **14**(21), 1800567.

9 A. Huang, W. Zhou, A. Wang, M. Chen, Q. Tian and J. Chen, Molten salt synthesis of α-MnO_2/Mn_2O_3 nanocomposite as a high-performance cathode material for aqueous zinc-ion batteries, *J. Energy Chem.*, 2021, **54**, 475–481.

10 X. Liu, J. Han, J. Deng, S. Imhanria, Z. Ren and W. Wang, Prussian blue analogue derived Pd-Co composite bifunctional electrocatalyst for Zn–air battery, *J. Alloys Compd.*, 2020, **832**, 154896.

11 Q. Ni, H. Jiang, S. Sandstrom, Y. Bai, H. Ren, X. Wu, Q. Guo, D. Yu, C. Wu and X. Ji, A $Na_3V_2(PO_4)_2O_{1.6}F_{1.4}$ Cathode of Zn-Ion Battery Enabled by a Water-in-Bisalt Electrolyte, *Adv. Funct. Mater.*, 2020, **30**(36), 2003511.

12 Y. Cheng, L. Luo, L. Zhong, J. Chen, B. Li, W. Wang, S. X. Mao, C. Wang, V. L. Sprenkle, G. Li and J. Liu, Highly Reversible Zinc-Ion Intercalation into Chevrel Phase Mo_6S_8 Nanocubes and Applications for Advanced Zinc-Ion Batteries, *ACS Appl. Mater. Interfaces*, 2016, **8**(22), 13673–13677.

13 T. B. Schon, B. T. McAllister, P. F. Li and D. S. Seferos, The rise of organic electrode materials for energy storage, *Chem. Soc. Rev.*, 2016, **45**(22), 6345–6404.

14 N. Yesibolati, N. Umirov, A. Koishybay, M. Omarova, I. Kurmanbayeva, Y. Zhang, Y. Zhao and Z. Bakenov, High Performance Zn/LiFePO4 Aqueous Rechargeable Battery for Large Scale Applications, *Electrochim. Acta*, 2015, **152**, 505–511.

15 Z. Jian, W. Han, X. Lu, *et al.*, Superior electrochemical performance and storage mechanism of $Na_3V_2(PO_4)_3$ cathode for room-temperature sodium-ion batteries, *Adv. Energy Mater.*, 2013, **3**(2), 156–160.

16 H. Yan, M. Li, Y. Fu, S. Chen, Y. Wang and B. Zhang, Conductive polypyrrole-promoted $Li_3V_2(PO_4)_3$ nanocomposite for rechargeable lithium energy storage, *J. Phys. Chem. Solids*, 2022, **167**, 110787.

17 L. Wang, Z. Li, H. Xu, *et al.*, Studies of $Li_3V_2(PO_4)_3$ additives for the $LiFePO_4$-based Li ion batteries, *J. Phys. Chem. C*, 2008, **112**(1), 308–312.

18 Y. Jiang, Q. Zou, S. Liu, H. Zeng, L. Chen, Y. Xiang, J. Li, X. Wu, J. Wu and L. Xiong, The $Li_3V_2(PO_4)_3$@C materials prepared by freeze-drying assisted sol-gel method for an aqueous zinc ion hybrid battery, *J. Electroanal. Chem.*, 2021, **900**, 115685.

19 X. H. Rui, C. Li and C. H. Chen, Synthesis and characterization of carbon-coated $Li_3V_2(PO_4)_3$ cathode materials with different carbon sources, *Electrochim. Acta*, 2009, **54**(12), 3374–3380.

20 K. Wu and J. Yang, Synthesis of carbon coated $Li_3V_2(PO_4)_3$/reduced graphene oxide composite for high-performance lithium ion batteries, *Mater. Res. Bull.*, 2013, **48**(2), 435–439.

21 B. Zhang, X.-w. Wang and J.-f. Zhang, Novel synthesis of $LiMnPO_4 \cdot Li_3V_2(PO_4)_3$/C composite cathode material, *RSC Adv.*, 2014, **4**(90), 49123–49127.

22 F. M. Courtel, Y. Abu-Lebdeh and I. J. Davidson, $ZnMn_2O_4$ nanoparticles synthesized by a hydrothermal method as an

anode material for Li-ion batteries, *Electrochim. Acta*, 2012, **71**, 123–127.

23 M. Amedzo-Adore and J. I. Han, Chemically lithiated layered $VOPO_4$ by a microwave-assisted hydrothermal method and its electrochemical properties in rechargeable Li-ion batteries and supercapacitor applications, *J. Alloys Compd.*, 2022, **911**, 165067.

24 H. Altun and S. Sen, Studies on the influence of chloride ion concentration and pH on the corrosion and electrochemical behaviour of AZ_{63} magnesium alloy, *Mater. Des.*, 2004, **25**(7), 637–643.

25 A. Yaghtin, S. M. Masoudpanah, M. Hasheminiasari, A. Salehi, D. Safanama, C. K. Ong, S. Adams and M. V. Reddy, Effect of Reducing Agent on Solution Synthesis of $Li_3V_2(PO_4)_3$ Cathode Material for Lithium Ion Batteries, *Molecules*, 2020, **25**(16), 3746.

26 M. Ding, M. Zhao, H. Gong, Q. Zheng and X. Song, Novel High-Rate Performance of Dual Carbon-Coated $Li_3V_2(PO_4)_3$ Materials Used in an Aqueous Electrolyte, *Ind. Eng. Chem. Res.*, 2018, **58**(2), 790–797.

27 W. J. Tang, W. J. Peng, G. C. Yan, *et al.*, Effect of fluoroethylene carbonate as an electrolyte additive on the cycle performance of silicon-carbon composite anode in lithium-ion battery, *Ionics*, 2017, **23**, 3281–3288.

28 N. Suo, A. Sun, L. Yu, Z. Zuo, X. Zhao, W. Zhang, Y. Zhang, L. Shao and Z. Dang, Effect of Al^{3+} ion-substituted Ni–Mg–Co ferrite prepared by sol–gel auto-combustion on lattice structure and magnetic properties, *Appl. Phys. A: Solids Surf.*, 2020, **126**, 1–13.

29 A. Liu, Enhanced electrochemical performance of lithium vanadium phosphate as cathode by LiBOB/LiTFSI with additive in EC/EMC, *Ionics*, 2013, **20**(4), 451–458.

30 J. Cui, X. Wu, S. Yang, C. Li, F. Tang, J. Chen, Y. Chen, Y. Xiang, X. Wu and Z. He, Cryptomelane-Type KMn_8O_{16} as Potential Cathode Material-for Aqueous Zinc Ion Battery, *Front. Chem.*, 2018, **6**, 352.

31 M.-S. Choi, H.-S. Kim, Y.-M. Lee and B.-S. Jin, Enhanced electrochemical performance of $Li_3V_2(PO_4)_3$/Ag–graphene composites as cathode materials for Li-ion batteries, *J. Mater. Chem. A*, 2014, **2**(21), 7873–7879.

32 C. Wan, H. Liu, Y. Wang, S. Liu, B. Liang, X. Wu and J. Jiang, Comparison of electrochemical performance of vanadium phosphate lithium battery in different electrolyte, *Guangdong Huagong*, 2023, **50**(06), 10–13.

33 F. Wang, E. Hu, W. Sun, T. Gao, X. Ji, X. Fan, F. Han, X.-Q. Yang, K. Xu and C. Wang, A rechargeable aqueous Zn^{2+}-battery with high power density and a long cycle-life, *Energy Environ. Sci.*, 2018, **11**(11), 3168–3175.

34 H. B. Zhao, C. J. Hu, H. W. Cheng, J. H. Fang, Y. P. Xie, W. Y. Fang, T. N. Doan, T. K. Hoang, J. Q. Xu and P. Chen, Novel Rechargeable $M_3V_2(PO_4)_3$//Zinc (M = Li, Na) Hybrid Aqueous Batteries with Excellent Cycling Performance, *Sci. Rep.*, 2016, **6**, 25809.

35 C. Li, W. Yuan, C. Li, H. Wang, L. Wang, Y. Liu and N. Zhang, Boosting $Li_3V_2(PO_4)_3$ cathode stability using a concentrated aqueous electrolyte for high-voltage zinc batteries, *Chem. Commun.*, 2021, **57**(35), 4319–4322.

36 Z. Shihao, W. Xianwen, X. Yanhong, *et al.*, Manganese-based cathode materials for aqueous zinc ion batteries, *Prog. Chem.*, 2021, **33**(4), 649.

37 X. H. Rui, N. Ding, J. Liu, C. Li and C. H. Chen, Analysis of the chemical diffusion coefficient of lithium ions in $Li_3V_2(PO_4)_3$ cathode material, *Electrochim. Acta*, 2010, **55**(7), 2384–2390.

38 T. Ruan, S. Lu, J. Lu, J. Niu and R. Li, Unraveling the intercalation chemistry of multi-electron reaction for polyanionic cathode $Li_3V_2(PO_4)_3$, *Energy Stor. Mater.*, 2023, **55**, 546–555.

39 H. Huo, Z. Lin, G. Zhong, S. Lou, J. Wang, Y. Ma, C. Dai, Y. Xiong, G. Yin and Y. Yang, The origins of kinetics hysteresis and irreversibility of monoclinic $Li_3V_2(PO_4)_3$, *J. Energy Chem.*, 2022, **67**, 593–603.

40 Q. Zou, H. Zeng, L. Wang, Z. Liu, B. Liu, J. Li, L. Xiong, X. Wu and Y. Xiang, Efficient Recycling of Electrolytic Manganese Anode Mud for the Preparation of Cathode Materials for Aqueous Zinc Ion Batteries, *J. Electroanal. Chem.*, 2023, **928**, 117044.

41 Y. Li, H. Huang, J. Yu, Y. Xia, C. Liang, Y. Gan, J. Zhang and W. Zhang, Improved high rate capability of Li $[Li_{0.2}Mn_{0.534}Co_{0.133}Ni_{0.133}]O_2$ cathode material by surface modification with Co_3O_4, *J. Alloys Compd.*, 2019, **783**, 349–356.

42 S. Dong, Y. Zhou, C. Hai, J. Zeng, Y. Sun, Y. Shen, X. Li, X. Ren, C. Sun, G. Zhang and Z. Wu, Understanding electrochemical performance improvement with Nb doping in lithium-rich manganese-based cathode materials, *J. Power Sources*, 2020, **462**, 228185.

43 C. Wu, S. Cao, X. Xie, C. Guo, H. Li, Z. Li, Z. Zang, B. Chang, G. Chen, X. Guo, T. Wu and X. Wang, Architecture and performance of anion-doped Co-free lithium-rich cathode material with nano-micron combined morphology, *Chem. Eng. J.*, 2022, **429**, 132141.